

Tuning the optical properties and thermal stability of polymeric graphitic carbon nitride (g-C₃N₄) with inclusion of ZnS for an emissive layer.

Debashish Nayak

Ram Bilash Choudhary (✉ rbcism@gmail.com)

IIT(ISM) Dhanbad <https://orcid.org/0000-0001-9821-7109>

Research Article

Keywords: ZnS, g-C₃N₄, Optical, Thermal stability, Photoluminescence

Posted Date: May 10th, 2022

DOI: <https://doi.org/10.21203/rs.3.rs-1617008/v1>

License: © ⓘ This work is licensed under a Creative Commons Attribution 4.0 International License.

[Read Full License](#)

Tuning the optical properties and thermal stability of polymeric graphitic carbon nitride (g-C₃N₄) with inclusion of ZnS for an emissive layer.

Debashish Nayak¹ and Ram Bilash Choudhary^{1*}

¹*Nanostructured Composite Materials Laboratory, Department of Physics, Indian Institute of Technology (Indian School of Mines), Dhanbad, 826004, Jharkhand, India*

**Corresponding author: Ram Bilash Choudhary, rbcism@gmail.com*

Abstract

Luminescent polymeric graphitic composites have the potential to be efficient energy converters for sophisticated displays and light sources. Thermal condensation is used to synthesize g-C₃N₄-ZnS composites. The XRD, and FTIR analyses confirmed the synthesis of the pure host, filler, and composites. FESEM, and TEM images revealed that the ZnS nanosheets were evenly distributed over the g-C₃N₄ sheets. The addition of ZnS improves the thermal stability of g-C₃N₄. The optimized gZ15 band gap is determined to be 2.98 eV with a crystallite size of 4.2 nm and a micro stain of 35.42×10^{-3} . With a purity of 63.4 %, gZ15 demonstrated a significant rate of recombination in the blue region. All of the improved properties demonstrated that polymeric g-C₃N₄-ZnS was the optimum materials for usage in the active or emissive layer of optoelectronic devices.

Keywords

ZnS; g-C₃N₄; Optical; Thermal stability; Photoluminescence.

1 Introduction

Two-dimensional (2D) van der Waals (vdW) nanomaterials are currently attracting a lot of attention, due to their unique features in optics and electronics [1, 2]. Among the various possibilities for exploring attractive sustainable energy sources and technologies, nanostructure materials with their intense optical properties are the most appealing and promising materials for directly harvesting, converting, and storing renewable solar energy & Organic light emitting diode for generating sustainable and green energy, as well as a wide range of environmental applications [3]. Non-centrosymmetric features, such as triangular-shaped holes in graphene or monolayer or turbostratic stacking patterns in transition metal dichalcogenides (TMDs), can induce piezoelectric responses in two-dimensional (2D) layered materials [4]. There are many materials used in optoelectronics, from that polymeric graphitic carbon nitride ($g\text{-C}_3\text{N}_4$) has evolved as one of the most potential materials for optoelectronic applications due to its distinctive lattice, optical and electronic properties [5].

Polymeric Graphitic carbon nitride ($g\text{-C}_3\text{N}_4$) is a metal-free semiconductor with a 2D structure. $g\text{-C}_3\text{N}_4$ is a fascinating material with excellent mechanical strength, thermal conductivity, water resistance, and chemical inertness. Due to this properties it have major applications as a photoelectric converter, catalyst for organic synthesis, gas and fluorescent sensors, optoelectronic devices, field emitters, fuel cell electrode, and hydrogen storage material etc. [6, 7, 8]. Because of its easy synthesis process, unique structure, non-toxicity, high temperature resistance, chemical stability, and high rate of electron-hole recombination mechanism, $g\text{-C}_3\text{N}_4$ has significant benefits over other materials [9]. It may be produced by direct condensation of low-cost N-rich feed stocks like as melamine and urea. Heating in furnace is more effective and dependable, with benefits such as time savings, reduced energy consumption, and high economic feasibility. Because of its polymeric composition, it enables for easy modification by doping of metal, non-metal, metal sulfide and metal oxide semiconductors. It can increase visible light absorption as well as the lifespan of photo-generated electron-hole (e-h) due to quicker recombination [10]. Some recent study has showed that exfoliated thin layers of $g\text{-C}_3\text{N}_4$ can boost reactive sites, specific surface area, mass transferability, electron transport, light absorption, and photo catalytic activity, etc. [11].

Semiconductor nanocrystals are promising materials for their form and size-based electrical, structural, thermal, and optical properties, have piqued the curiosity of many researchers in recent years [12]. ZnS is a Wurtzite crystal structure broad and direct band gap compound semiconductor nanomaterial. It is widely utilized in light-emitting diodes, optoelectronics, field-effect transistors, and transparent films. ZnS nanosheets have recently been shown to have a variety of luminescence properties, including electroluminescence [13]. ZnS quantum dots are widely used in flat-panel displays and infrared windows due to their high exciton binding energy of 40 meV [14]. The incorporation of ZnS into the synthesis process helps to enhance the optical characteristics, structure, and thermal stability of pure $g\text{-C}_3\text{N}_4$. Many scientists and researchers have developed different methods for synthesizing composites for improving the properties of materials used in energy conversion and storage systems. The $g\text{-C}_3\text{N}_4\text{-ZnS}$ composites utilized for photo-degradation of organic dye under uv-vis light are explained by Palanisamy et al. [15]. Dai et al. synthesized the $g\text{-C}_3\text{N}_4\text{-ZnS}$ composites using a simple method that demonstrated outstanding photo stability [16]. Ghosh et al. created two distinct types of 2D $g\text{-C}_3\text{N}_4$ samples from the same starting material (melamine), each with its own set of optical and optoelectrical characteristics, just by altering the post-growth annealing ambiance [17]. Mixture of quantum dots and ZnS nanoparticles used as emissive layer in LED was described by Song et al. [18]. Until now, no one has explained the

impact of zns in the g-c3n4-zns composites, therefore it is a huge step to employ the g-C₃N₄-ZnS composites in the emissive layer with the materials' enchaining capabilities.

In this article, we describe the synthesis of polymeric g-C₃N₄-ZnS nanocomposite with the variation of the ZnS wt % from 5 to 20. The synthesized materials were structurally, morphologically, thermally and spectroscopically characterized using XRD, FTIR, FESEM, TEM, TGA, DTA, DSC, Photoluminescence, and Ultraviolet-Visible (UV-vis) methods. The variations in the composites were noticed and thoroughly discussed in the section below, as well as how it is employed for the emissive layer (active layer) in optoelectronic devices.

2 Experimental

2.1 Materials

All of the ingredients used in this synthesis are bought and not purified further. The percentage of the purification of the chemicals are more than 99 % and all the chemicals are purchased from Alfa Aesar, and TCI. Zinc nitrate hexahydrate (Zn(NO₃)₂).6H₂O (MW=297.49), thiourea (CH₄N₂S) (MW=76.12), ethylenediamine (C₂H₈N₂) (MW=60.1) were used for the synthesis of ZnS. In the process of synthesis for g-C₃N₄, melamine monomer (C₃H₆N₆) (MW=126.12) was used. In the whole process deionized water, acetone, and ethanol were used for the synthesis and washing purpose to avoid the contaminated.

2.2 Synthesis of ZnS

Zinc sulphide nanoplates were created using the solvothermal process. A 1:3 M combination of zinc nitrate hexahydrate and thiourea was dissolved in 60 ml of ethylenediamine solution while being magnetically stirred. The solution was sonicated for 1 hour before being transferred to a stainless steel autoclave lined with Teflon and held at 180 °C for 48 hours. The precipitate was then centrifuged and washed many times with distilled water and ethanol. The white material is then collected and dried overnight in a vacuum oven. The white powder was then annealed for 2 hours at 400 °C in a muffle furnace. When the temperature of the material was reduced to room temperature, the color of the material changed slightly to a brilliant grey tint, and the entire sample was collected and characterized.

2.3 Synthesis for g-C₃N₄-ZnS nanocomposite

g-C₃N₄-ZnS nanocomposites were synthesized through thermal condensation of melamine with the presence of ZnS in a muffle furnace as shown in the fig.1. In four separate beaker, 5 g of melamine was taken with 30 ml of DI water. Then (5, 10, 15, 20) wt% of ZnS added into the solution separately at constant stirring. After 2 hrs the temperature gradually increase to 80 °C for five hrs at continuous starring. Then the whole solution were kept in the oven at 120 °C for 12 hrs to evaporate all the water from the solution. Then the samples were collected, and ground it properly for 2hrs to get well mixture powder sample. All the four sample, typically placed in four different alumina crucible with lid cover and heated to 550 °C in a muffle furnace at a heating ramp of 2.5 °C/min and maintained at 550 °C for 3 hours. After the system had naturally cooled to room temperature, the final yellow color product was crushed into powder, cleaned with deionized water

and ethanol, and then dried in an air dry oven at 60°C for 6 hours for further characterization. In similar process the pure g-C₃N₄ was synthesized with out the presence of the ZnS.

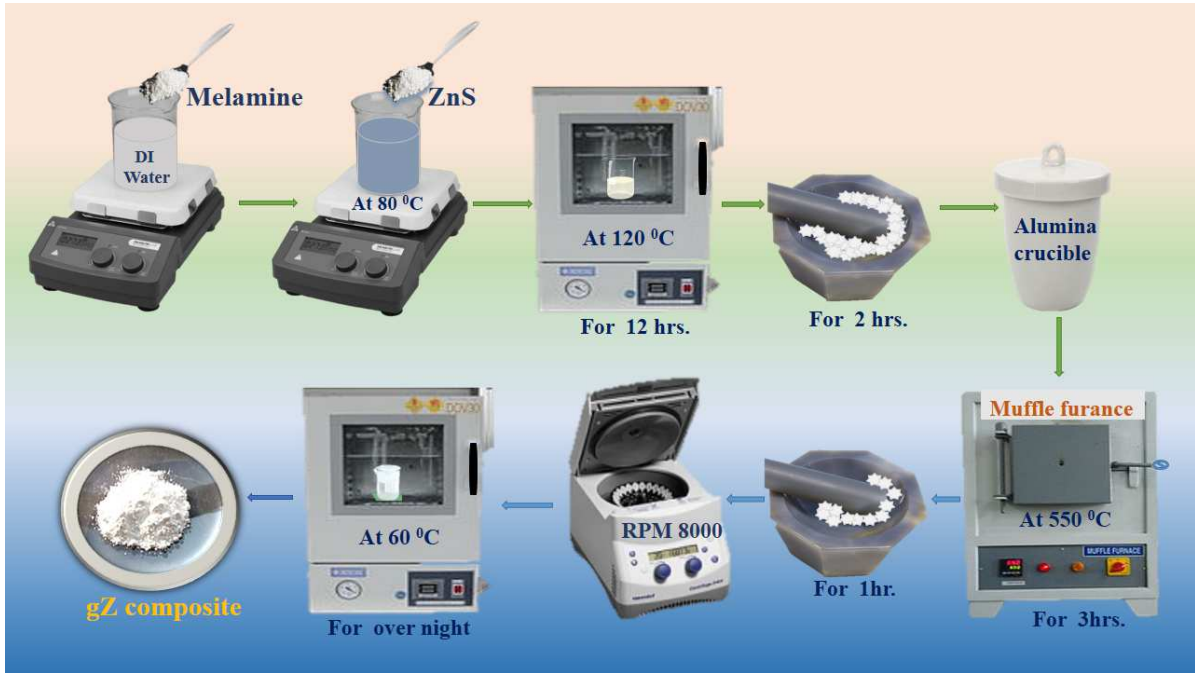


Figure 1: Schematic representation for synthesis of gZ nanocomposite.

2.4 Characterization Technique

Table 1 contains information on the model and instrument utilized in the characterization of the nanocomposite.

Table 1: The model and instrument used for the characterization study.

Characterization	Instrument	Make/Model
X-ray analysis	HRXRD	Rigaku/Smartlab
FTIR	FTIR spectrophotometer	PERKIN ELMER Spectrum 2.0
Surface morphology	FESEM	Zeiss/Supra 55
In depth morphology	HRTEM	Thermo Scientific/ Talos F200X G2
Elemental analysis	XPS	PHI/5000 versa probe III
Thermal Analysis	TGA/DSC/DTA	STA 6000 (Perkin Elmer)
Absorbance and Band gap	UV-VIS Spectrophotometer	Agilent/Cary 500

3 Result and Discussion

3.1 Formation and morphological study

As shown in Fig. 2(a), X-ray diffraction was applied to quantify the crystal phase and purity of as-synthesized g-C₃N₄, ZnS, and g-C₃N₄-ZnS nanocomposite materials. All of the peaks in the g-C₃N₄ XRD pattern are well matched with the JCPDS data (JCPDS-87-1526). The XRD pattern of pure g-C₃N₄ (at 550 °C) indicated a bigger diffraction peak at around 27.7 ° and a smaller one at around 13 °. The 13 ° diffraction peak is indexed as (1 0 0) plane and corresponds to an in-plane structural packing motif of tri-s-triazine units. The (0 0 2) plane of the conjugated aromatic system stacking is indexed at 27.7 ° and corresponds to inter-layer stacking of aromatic segments separated by 0.32 nm [19]. At the same time, Wurtzite ZnS has a hexagonal tightly packed structure in which the Zn atom is tetrahedrally coordinated with four sulfide atom, and each sulfide atom binds four zinc atoms. As a result, hexagonal Wurtzite ZnS has two polar faces, one with just Zn ions and the other with only S ions. These two faces are alternately layered along the c-axis. The coordinate number of Zn⁺² ions and S⁻² ions is 4. As a result, this structure has a 4:4 coordination. The XRD pattern of the synthesized ZnS shows diffraction peak at 26.94 °, 28.5°, 30.53°, 39.62°, 47.56°, 51.77°, 57.63°, and 72.95° correspond to the (0 0 2), (0 1 0), (0 1 1), (0 1 2), (1 1 0), (0 1 3), (1 1 2), and (0 2 3) planes respectively which are well matched with the ICDD: 98-004-3597 data base. Using Bragg's law, we can calculate different parameter of the sample given below,

$$2d \sin\theta = n\lambda \quad (1)$$

where n is the diffraction order (usually used first order n =1), λ is the X-ray wavelength, and d is the inter-planar distance. The inter-planar spacing d in hexagonal ZnS is linked to the lattice constants a, c, and miller indices h, k, and l which is related to the below equation [20],

$$\frac{1}{d_{hkl}^2} = \frac{4}{3} \left(\frac{h^2 + hk + k^2}{a^2} \right) + \frac{l^2}{c^2} \quad (2)$$

By taking all the values of the ZnS we calculated the lattice parameters for ZnS. Using above equation we found a = b = 3.606, and c = 6.604 Å, hence c/a = 1.8313 and unit cell volume is 74.37 Å³. The crystallite size of synthesized materials determined using the Debye-Scherrer formula using the equation below [21],

$$D = \frac{k\lambda}{\beta_{hkl} \cos\theta} \quad (3)$$

where λ is the X-ray wavelength of the Cu-K α line, D is the average crystallite size, and k is the Scherrer's constant (shape factor) of 0.91. β represents the peak's full width at half maximum (FWHM). The dislocation density was also calculating using below equation [22],

$$\text{Dislocation density, } \delta = \frac{1}{D^2} \quad (4)$$

where D is the average crystallite size. All the parameter of the materials at prominent peak were calculated and tabulated in the table no.2. Dislocation density of the materials increased with the

addition of the ZnS in to the host materials. It was obvious from the XRD data that the materials were well synthesized for oled and optical applications.

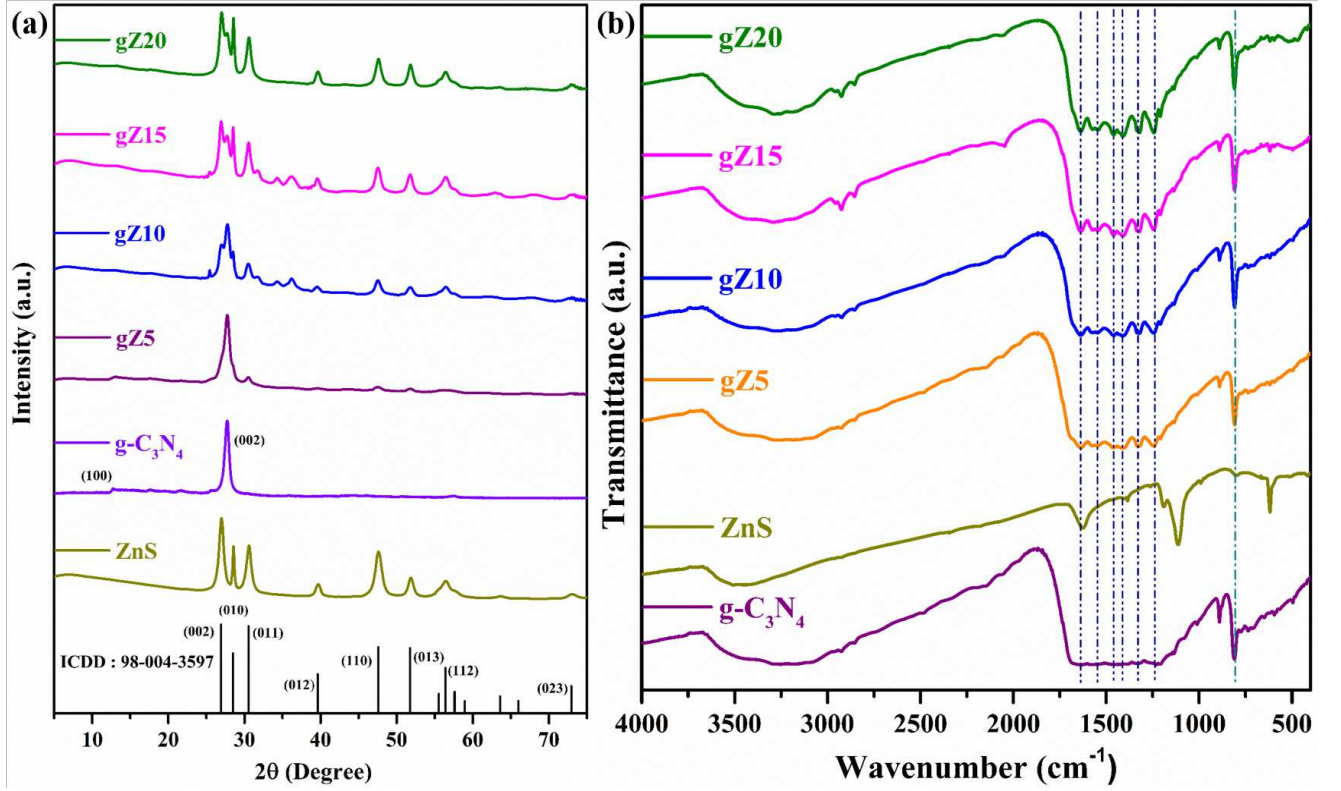


Figure 2: (a) XRD patterns of as-prepared different sample, (b) FTIR spectra of synthesized sample.

Table 2: Strutral parameters and crystalline size of synthesized sample

Synthesized materil	Prominent peak (2θ)	Crystallite size (nm)	Micro strain (ϵ)($\times 10^{-3}$)	Inter-planer distance d_{hkl} (Å)	Dislocation denstiy (δ) lines/m ²
g-C ₃ N ₄	27.7	11.6	12.53	3.22	8.6×10^{16}
ZnS	26.98	11	13.23	3.30	8.2×10^{15}
gZ5	27.6	8	18.16	3.23	1.5×10^{16}
gZ10	27.6	5	29.29	3.23	04×10^{16}
gZ15	26.99	4.2	35.42	3.30	5.6×10^{16}
gZ20	27.4	4	36.43	3.26	6.2×10^{16}

FTIR spectroscopy was used to analyze all of the synthesized materials, and the findings are represented in Fig.2(b). All of the functional groups found in the sample were thoroughly investigated. Major peaks in the spectra of g-C₃N₄ and related nanocomposites may be seen about 3290 cm⁻¹, 1250-1650 cm⁻¹, and 809 cm⁻¹. The N-H groups' stretching mode results in a broad band in the 3290⁻¹ area [23]. Many peaks are visible in the area between 1250 and 1650 cm⁻¹, which are linked to the existence of C-N stretching vibrational mode [24, 25]. The peaks

at 809 cm^{-1} which attributed to the regular breathing mode of the s-triazine or heptazine ring vibrations [26]. In the FTIR spectra of ZnS, a large wide peak in the range of $3200\text{-}3500\text{ cm}^{-1}$ is ascribed to the existence of a vibrational O-H group caused by the sample's surface absorbed water molecules [27]. Peak near 1628 cm^{-1} due to the presence of O-H bending of water. There are many peaks in the region between $400\text{ to }650\text{ cm}^{-1}$ in ZnS due to the Zn-S bond where the peak shown at 670 cm^{-1} is attributed to the S-S band. FTIR analysis provides information that is very well satisfied with the XRD data, and the formation of the polymeric composites was confirmed.

The optical examination employed field emission scanning electron microscopy (FESEM) and transmittance electron microscopy (TEM) studies to explore the surface morphological nature of the as synthesized materials. FESEM pictures of the synthesized materials are shown in Fig.3. Fig. 3(a) depicts a FESEM picture of $\text{g-C}_3\text{N}_4$ irregular particles with a lamellar structure. Fig. 3(b) depicts the hexagonal sheet-like structure of pure ZnS. Fig. 3(c-f) depicts the morphology of the gZ5, gZ10, gZ15, and gZ20 respectively. In the case of $\text{g-C}_3\text{N}_4\text{-ZnS}$ nanocomposites, it is clear that irregular ZnS nanosheets were deposited on the surface of $\text{g-C}_3\text{N}_4$, resulting in hetero-structured gZ nanocomposites. When ZnS was added to the melamine monomer and the thermal polycondensation process was carried out for formation of composites, the morphology of the composites changed and the hexagonal structure of the ZnS was well spread across the host material's surface. The presence of the filler in the composites were conform through the Energy dispersive X-ray spectroscopy (EDS) in a selected area of the FESEM image.

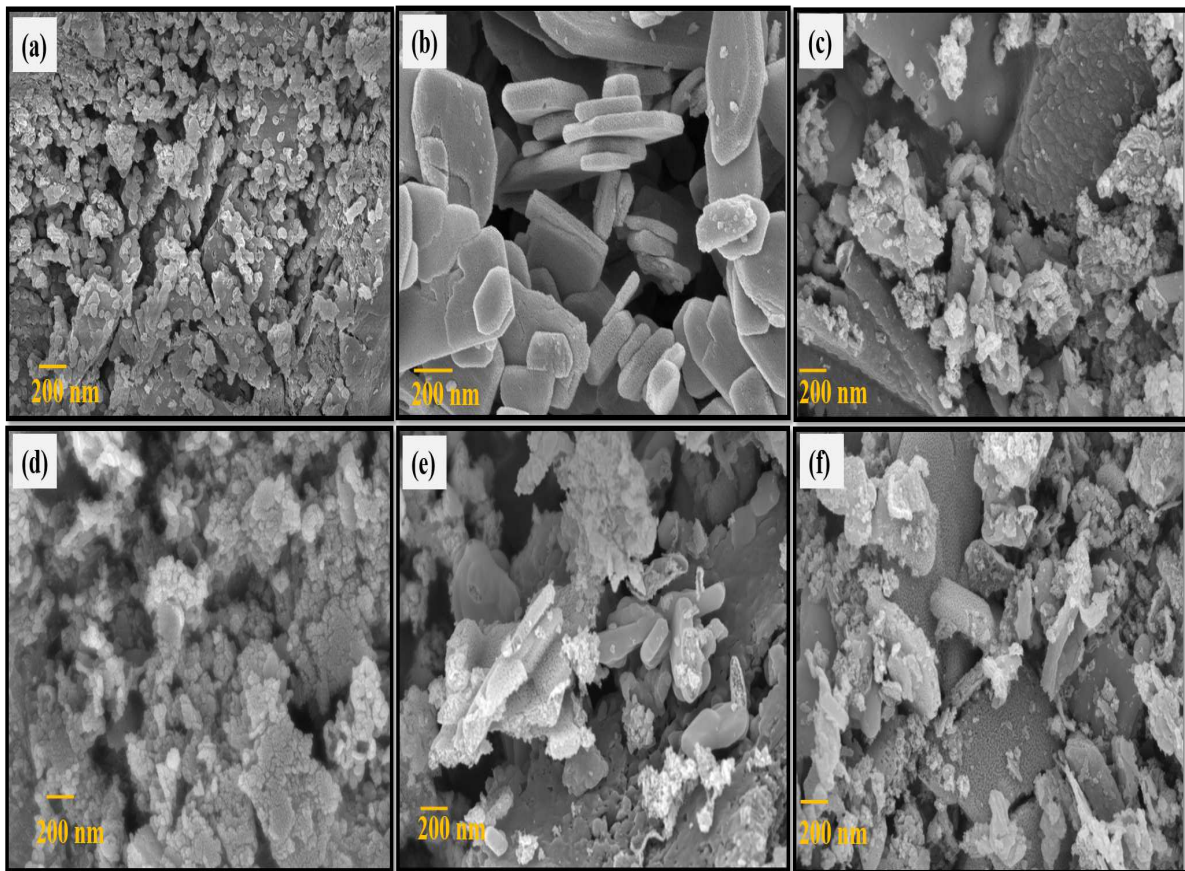


Figure 3: FESEM images for (a) $\text{g-C}_3\text{N}_4$, (b) ZnS, (c) gZ5, (d) gZ10, (e) gZ15, (f) gZ20

The EDS of host $g\text{-C}_3\text{N}_4$, ZnS, and the optimized gZ15 composite are depicted in 4. The pure $g\text{-C}_3\text{N}_4$ demonstrates the presence of carbon, nitrogen, and oxygen as specified in (a, b). The EDS of pure ZnS shown the formation of the ZnS and the presence of the zinc and sulphur in the metal sulfide (c-d). The presence of zinc, sulphur, carbon, and nitrogen in the composite indicates that the ZnS was dispersed throughout the gZ15 composite (e-f). EDS confirmed the synthesis of the composites as well as the purity and absence of impurities in the composites.

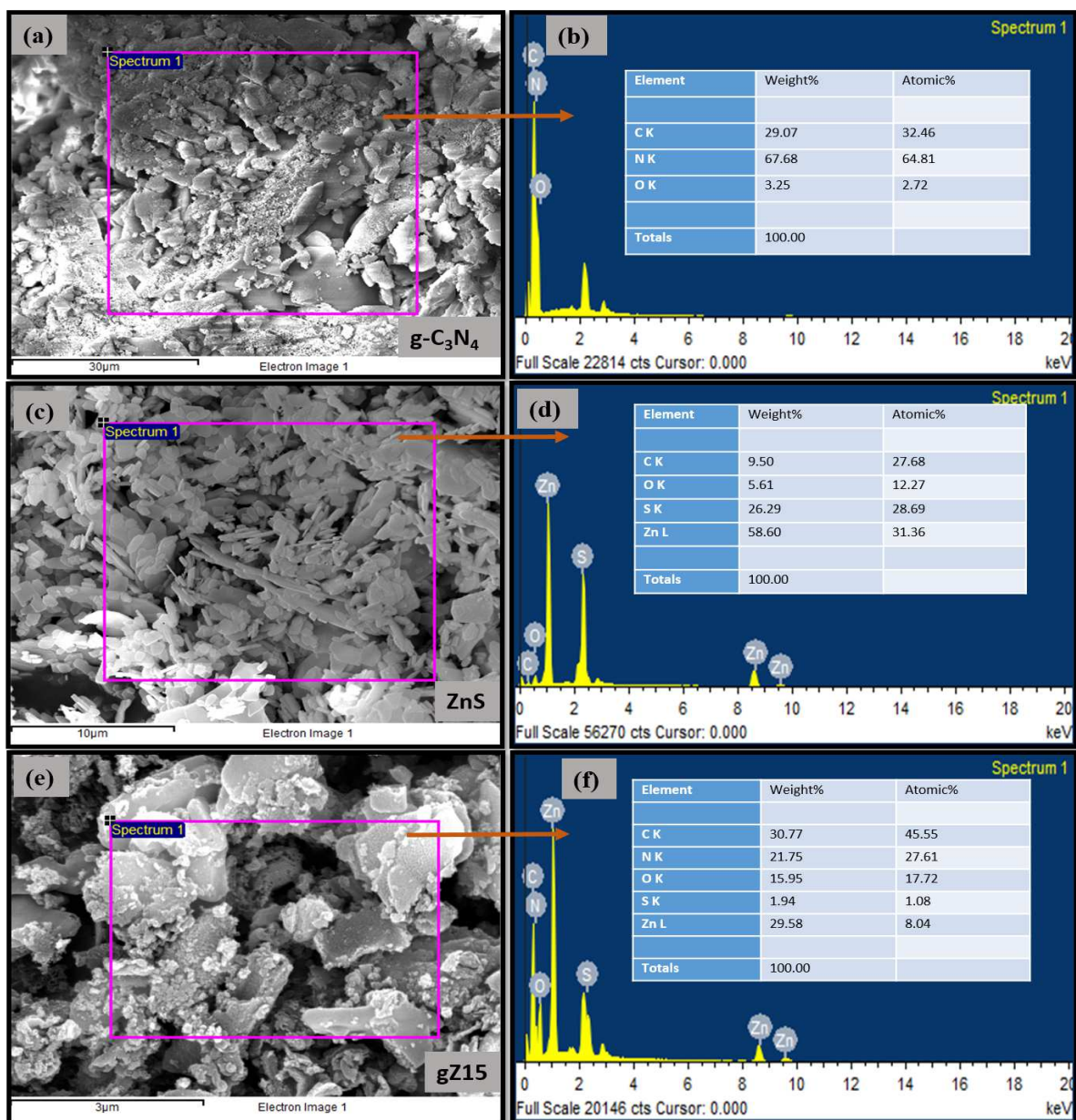


Figure 4: EDX analysis of (a-b) $g\text{-C}_3\text{N}_4$, (c-d) ZnS, (e-f) gZ15

HR-TEM images of $g\text{-C}_3\text{N}_4$, ZnS, and gZ15 were characterized for better morphological studies, as shown in fig. 5. The polymeric $g\text{-C}_3\text{N}_4$ displays a sheets-like structure in fig. 5(a). Fig. 5(b) depicts ZnS's hexagonal structure. Fig. 5(c) depicts the presence of ZnS and $g\text{-C}_3\text{N}_4$ in gZ15 composites. The ZnS was evenly distributed across the gZ15's surface. The black patch were

shown in the TEM images of the composites were ZnS where the white sheet like structure were g-C₃N₄. Fig. 5(d) shows the selected area electron diffraction (SAED) pattern of the composites. The polycrystalline nature of the materials were conformed through the SAED lattice fringes. The planes estimated from the SAED pattern in TEM] images are nicely matched with the materials' xrd pattern. as a result of this it provides substantial information for the formation of composites.

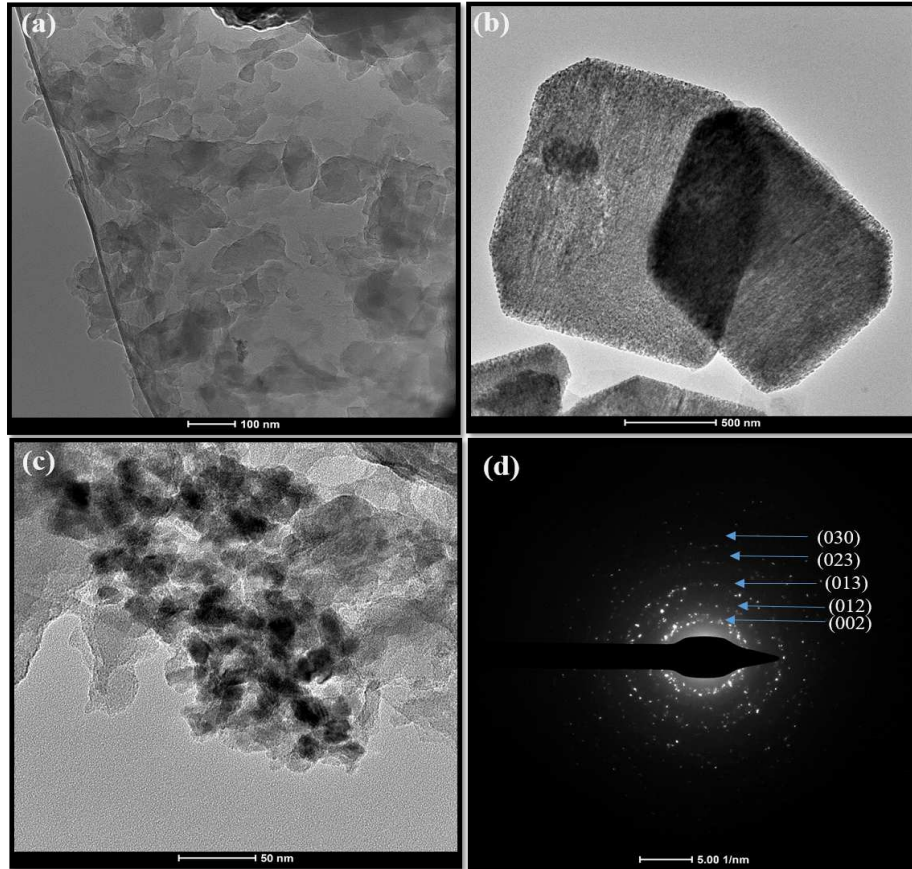


Figure 5: HR-TEM images for (a) g-C₃N₄, (b) ZnS, (c) gZ15, (d) SAED pattern of gZ15.

The chemical composition of the g-C₃N₄-ZnS hetero-junctions and the interaction of ZnS with the g-C₃N₄ and electronic and oxidation state were investigated further using XPS analysis in the binding energy range of 0-1200 eV [28]. The entire XPS spectra of the g-C₃N₄-ZnS (gZ15) hetero-junctions are shown in Fig. 6. The survey scan (6(a)) shows the presence of the Zn, S, C, N. At the same time a faint O 1s signal was also noticed, which can be attributed to a little quantity of O₂ adsorbed on the sample's surface during the polymerization process. The C 1s peaks 6(b) were deconvoluted into three distinct peaks at 284.5 eV, 286 eV, and 288 eV, respectively, attributable to the hybridized sp² C-C bond, C-N bond, and C-N=C bond. There are four deconvoluted peaks in the binding energy part of the N 1s spectrum as shown in fig. 6(c). Peaks at 398.7 eV, 397.9 eV, 399.2 eV, and 400.4 eV are assigned to the -C=NH, C=N-C, C-NH₃, and graphitic N, respectively, confirming the triazine units' sp² linked N atoms. The tertiary N in N-(C)₃, as well as the N atoms in aromatic hetero-cycles, are all linked to π -excitation and charging effects of g-C₃N₄, respectively. Fig.6(d) shows the high-resolution spectra of Zn 2p. Zn²⁺ electronic states (Zn 2p_{3/2} and Zn 2p_{1/2}, respectively) are represented by the two peaks at 1022.7 and 1045.7

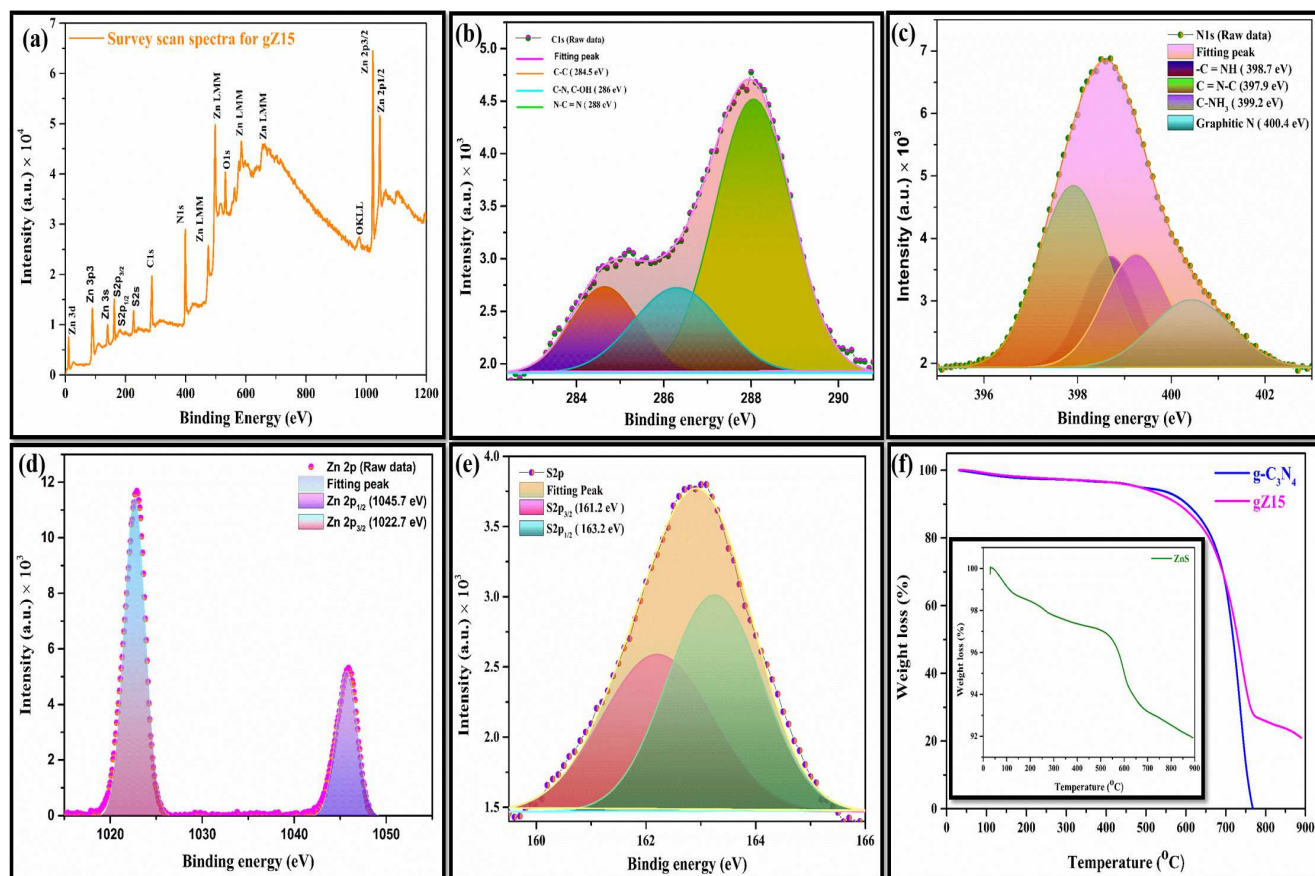


Figure 6: XPS survey scan spectra for (a) gZ15; detailed scan for (b) C 1s electronic state, (c) N 1s electronic state, (d) Zn 2p electronic state, (e) S 2p electronic state; (f) TGA analysis for the synthesized sample.

eV. The bivalent state of Zn is shown by the difference of ~ 23 eV between the two core level components of Zn 2p_{3/2} and Zn 2p_{1/2}. Furthermore, the main sulphur species on the surface of can be divided into two main characteristic peaks at 161.2 eV and 163.2 eV, ascribed to the S 2p_{3/2} and S 2p_{1/2}, respectively, in good agreement with the energy of the Zn-S bond, as shown by the fitting of the XPS spectrum of sulphur S 2p peaks fig.6(e). The XPS examination clarifies the oxidation and material composition of the composites. which shown that these materials are appropriate for the emissive layer of oleds and the active layer of optoelectronic devices.

3.2 Thermal Analysis

In this method, the physical characteristics of materials are monitored as a function of a controlled temperature change. Weight loss due to heating, melting point, heat and energy transfers, change in shape, changes in dimension, and changes in viscoelastic characteristics are all part of this process. The thermal stability of g-C₃N₄, ZnS, and gZ15 composites was shown in Fig. 6(f). The evaporation of the adsorbed moisture in the sample is attributed to the minor weight of ~ 1 % weight loss below 200 °C. Meanwhile, weight loss between 200 and 300 °C is due to citric acid breakdown. The deterioration of g-C₃N₄ began at 600 °C and ended at 770 °C, as shown. However, because of the presence of ZnS in the composites, the sample % degraded less than the pure in the

case of the gZ15. In the temperature range of 0 to 900 degrees, pure ZnS lose around 8% of their weight. It is apparent that ZnS has more thermal stability than pure g-C₃N₄, hence adding ZnS to the g-C₃N₄-ZnS (gZ15) composites boosts the stability when compared to the host materials.

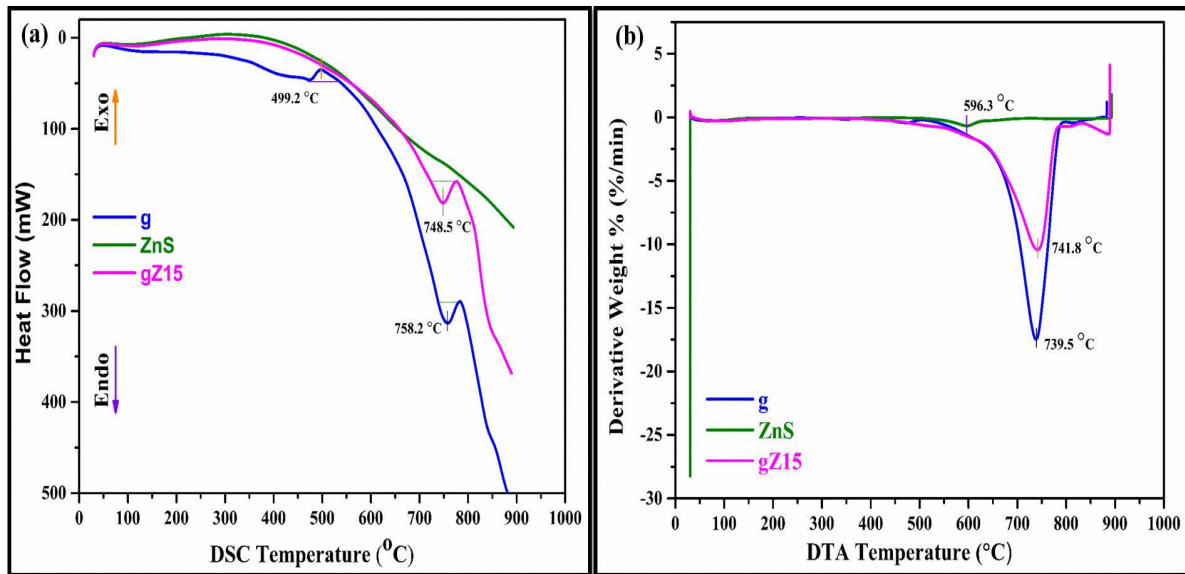


Figure 7: (a) DSC analysis for the g, ZnS and gZ15; (b) DTA analysis for the g, ZnS and gZ15.

Differential scanning calorimetry may be used to better understand how polymers behave when heated. This may also be used to characterize a polymer composite's melting and crystallization temperatures. The glass transition of the synthesized materials is shown in fig. 7(a), whereas g-C₃N₄ displays an exothermic peak at 499.2 °C, which is ascribed to the crystallization of the materials. A dip endothermic peak was seen at 758.2 °C, which was attributable to the melting of the components. The melting point of gZ15 was found to be about 748.5 °C. TGA, DSC, and DTA analyses confirmed that gZ composites were more thermally stable than other pure materials, allowing them to be employed in optoelectronic devices.

3.3 Spectroscopy Analysis

The optical properties of synthesized polymeric composites, in the 200-800 nm range were investigated using Ultra Violet -visible diffuse reflectance spectroscopy.

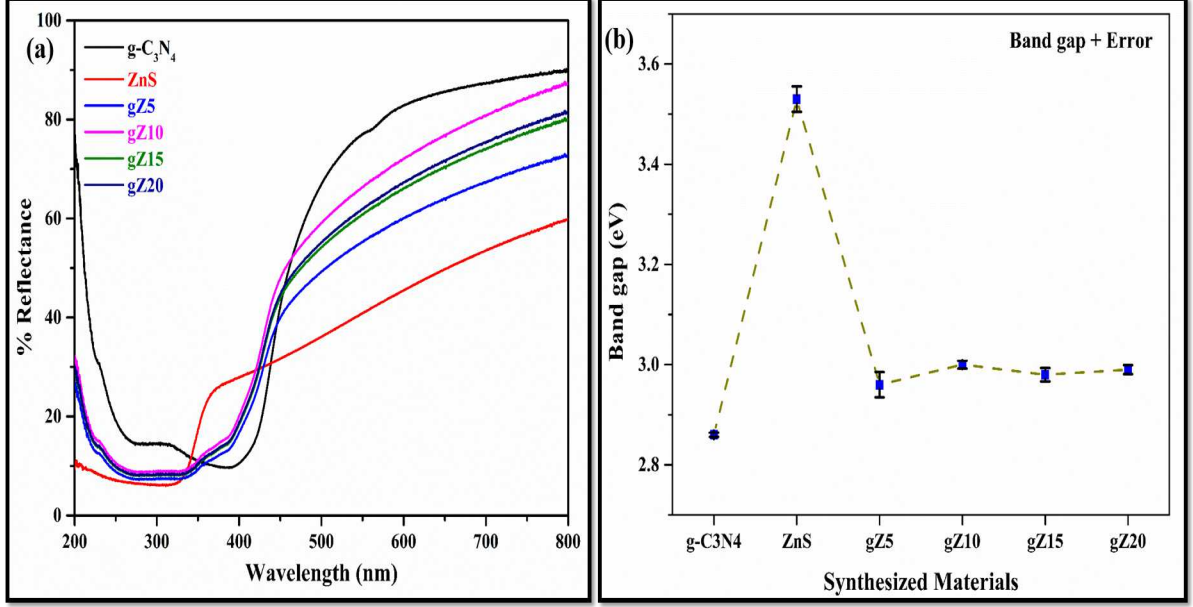


Figure 8: (a) Reflectance spectra of host, filler and their composites; (b) Band gap value and error calculation.

The reflectance spectra of g-C₃N₄, ZnS, and gZ nanocomposites are shown in Fig.8(a). Because the scattering component cannot be ignored in powder materials, optical absorption spectroscopy is not an effective technique for determining the value of E_g . Diffuse reflectance spectroscopy (DRS) is an improved way of calculating the band gap. The comparable Tauc graphs may be created using DRS by computing the Kubelka-Munk or re-emission function, ($F(R_\infty)$), using Eqs. (5), (6), and (7) given below [29]:

$$R_\infty = \frac{R_{Sample}}{R_{Standard}} \quad (5)$$

$$F(R_\infty) = \frac{(1 - R_\infty)^2}{2R_\infty} = \frac{K}{S} \quad (6)$$

where R_∞ is the diffuse reflectance of the sample "infinite thickness," implying that the supporting material has no contribution, and S & K are the absorption and scattering K-M coefficients.

$$F(R_\infty)h\nu = \beta(h\nu - E_g)^n \quad (7)$$

Where $F(R_\infty)$ is the Kubelka-Munk function, $h\nu$ is the photon energy of incident radiation in eV, β is the constant depending on the type of transition, E_g is the optical band gap (eV), and n is the index related to the nature of the electronic transition, where the value of n is 3, 3/2, 2, and 1/2 for indirect forbidden, direct forbidden, indirect allowed, and direct allowed electronic transitions, respectively. Although the Tauc method's foundations are well-established, success in determining E_g typically rests on the analyst's experience. The value of the band gap is calculated from the plot of energy ($h\nu$) vs $[F(R_\infty)h\nu]^{1/n}$ by extrapolating the straight line of this curve at $[F(R_\infty)h\nu]^{1/n} = 0$. In this case, n is the band gap transition dependent exponent, whose value is determined by whether the band gap transition is direct or indirect, as well as whether the transition is allowed or disallowed. Plotting $[F(R_\infty)h\nu]^{1/n}$ vs energy $h\nu$ yields the band gap. n should be considered as

1/2 for the straight band gap transition of g-C₃N₄, ZnS and gZ nanocomposites. The band gap value of the as synthesized materials shown in fig.9. The value for the band gap of the composites slightly increases to the host materials due to the atomic vibrations increase which leads to larger inter-atomic spacing. At the time of calculating the band gap of the material, error calculations are also performed, as shown in fig.8(b).The optimized materials had a band gap of 2.98 eV, which was appropriate for the emissive layer. Table 3 summaries the results of all band gap calculations.

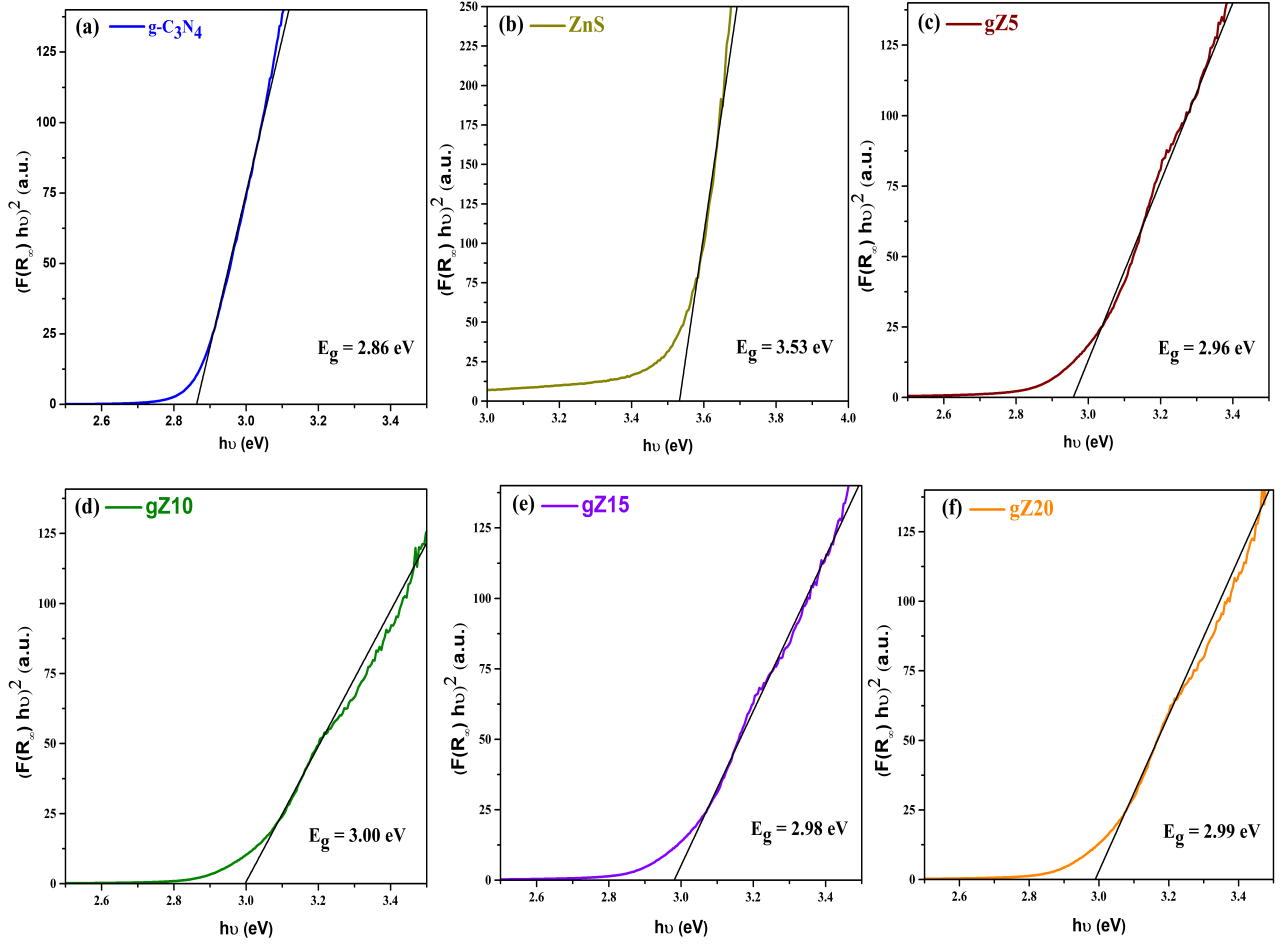


Figure 9: Band gap values for (a) g-C₃N₄, (b) ZnS, (c) gZ5, (d) gZ10, (e)gZ15, (f) gZ20.

Urbach energy (E_c) measures the degree of absorption edge smearing produced by structural and external lattice disordering. The Urbach empirical rule, which is provided by the equation, connects Urbach energy to absorption coefficient (α) and photon energy ($h\nu$) in the low photon energy range.

$$\alpha = \alpha_0 \left(\frac{h\nu}{E_c} \right) \quad (8)$$

where ' α_0 ' is a constant and ' E_c ' is the width of the band tail, commonly known as the Urbach energy. Taking logarithm on both sides of equation (8) provides a straight line, the equation of which is:

$$\ln \alpha = \ln \alpha_0 \left(\frac{h\nu}{E_c} \right) \quad (9)$$

As a consequence, the Urbach energy may be estimated from the straight line slope by plotting $\ln(\alpha)$ along the Y-axis and photon energy ($h\nu$) along the X-axis, as shown in fig. 10. The Urbach energy is obtained by taking the reciprocal of the linear component of the slope of the curve, which is calculated and reported in table no.3. The refractive index (n_0) of the synthesized materials is shown in table 3, which was calculated using the following relation,

$$\frac{n_0^2 - 1}{n_0^2 + 1} = 1 - \sqrt{\frac{E_g}{20}} \quad (10)$$

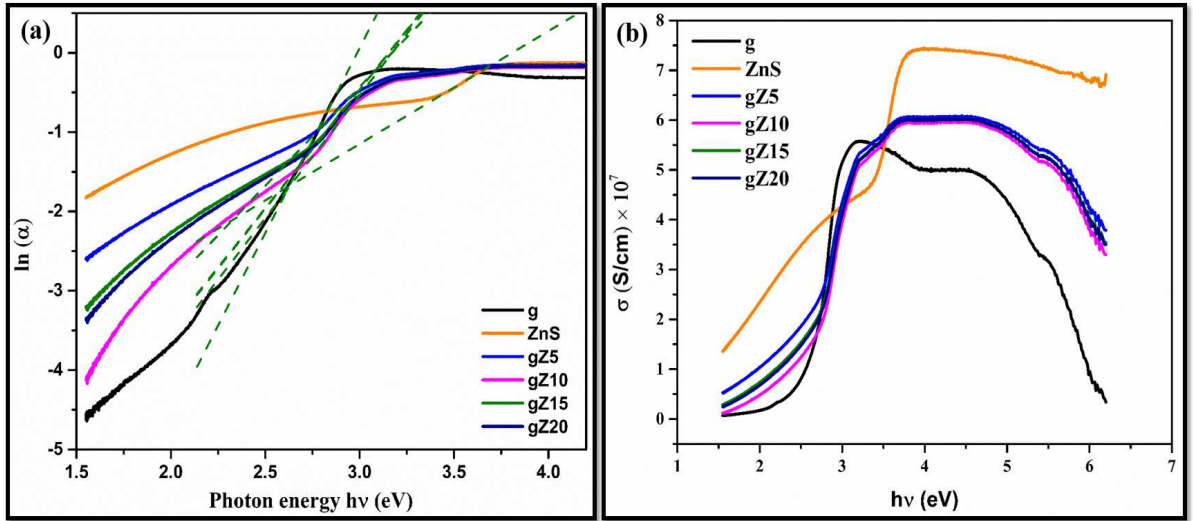


Figure 10: (a) Urbach energy for the synthesized materials, (b) Optical conductivity for g, ZnS and their composites.

The optical response of a material is often studied in terms of optical conductivity (σ), which is provided by the relationship,

$$\sigma = \frac{\alpha n_0 c}{4\pi} \quad (11)$$

where c denotes the speed of light, α the absorption coefficient, and n_0 the refractive index. It is apparent that the optical conductivity of a material is directly proportional to its absorption coefficient and refractive index.

At ambient temperature, the PL spectra of g- C_3N_4 (g) and gZ nanocomposites are exhibited in Fig.11(a). The recombination and separation of photo-generated electrons and holes was studied using PL spectra with an excitation wavelength of 325 nm. Because of the greater charge recombination rate and presence of the π state of g- C_3N_4 [30], the PL spectra of host g- C_3N_4 (g) exhibits an intense emission peak about 460 nm, indicating vivid blue. Figure 11(b) depicts the emission

Table 3: Optical value calculation for the synthesized materials.

Synthesized Materials	Band gap (eV)	Urbach energy (meV)	Refractive index (n_0)
g	2.86	214.6	2.074
ZnS	3.53	704.2	1.932
gZ5	2.96	401.6	2.049
gZ10	3.00	323.6	2.040
gZ15	2.98	333.3	2.044
gZ20	2.99	334.5	2.042

band at 390, 520, 570, and 625 nm, which shows deep purple, green, yellowish green, and orange red, respectively. The emission band at lower wavelength as a result of the sulphur vacancy trap state mediated process of radioactive recombination [15]. The addition of ZnS to pure g- C_3N_4 causes a red shift as the intensity increases. As the concentration of ZnS in the composites grew, the PL intensity steadily increased to a point, then decreased for gZ20 and furthermore. When compared to pure, the emission band intensity of gZ5, gZ10, and gZ15 increases. The greatest intensity, gZ15, was optimized for this work. Because of the separation of the electron and hole in the gZ20 nanocomposite, a highly quenching process occurs, indicating a high photocatalytic reaction.

Based on the trapping process, the Shockley - Read - Hall (SRH) model describes the statistics behind the recombination and production of holes and electrons in semiconductors [31]. The movement of electrons from the valence band (VB) into the conduction band (CB) is referred to as electron-hole pair production. A charge current will be generated as a result of the production of a free hole and an electron in the CB and VB, respectively.

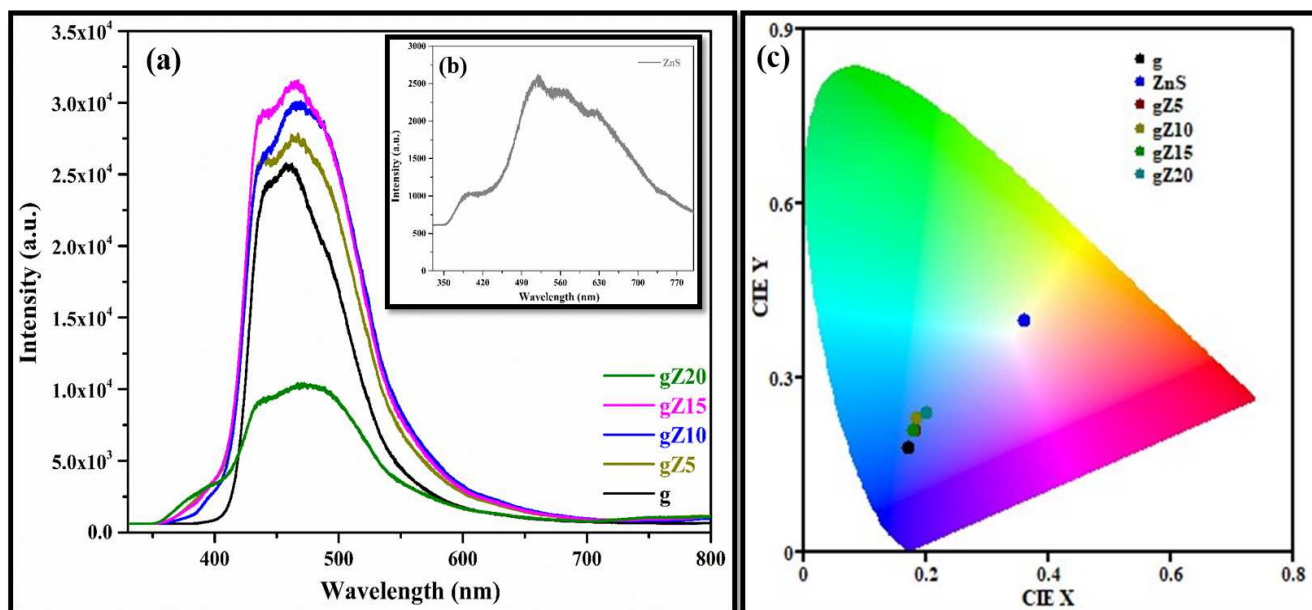


Figure 11: Room temperature PL spectra of (a) gZ nanocomposites, (b) ZnS and (C) CIE spectra of synthesized materials

Fig.12 showed the energy level diagram for the gZ composite. In this case, ZnS is stimulated by a wavelength of 325 nm, and electrons travel to the upper level, where the excited vibrational levels are in the conduction band. Through the charge transfer mechanism, this excited wavelength is transferred to the σ^* state of g- C_3N_4 material. After the exciton life period, the electron released energy via a non-radiative transition to enter the π^* and Nitrogen (L.P) states. This is the energy level diagram for light emission in gZ composites for emissive layer materials.

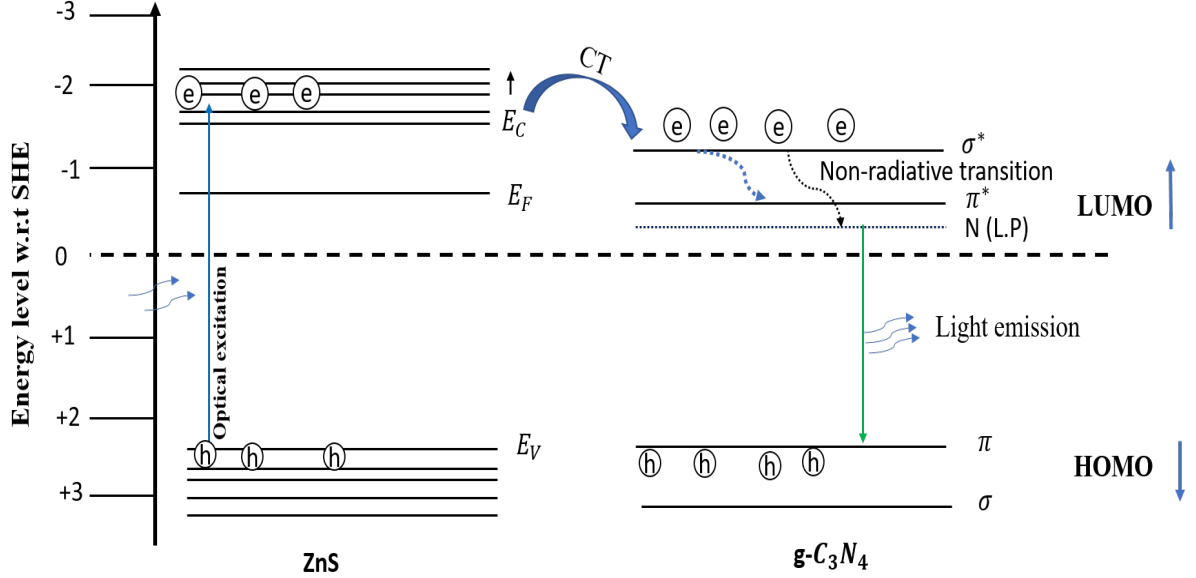


Figure 12: Energy level diagram for gZ composite.

The apparent emitted color of the produced luminescent materials may be predicted using CIE (Commission Internationale de l'éclairage) color coordinates as a function of excitation wavelength. CIE color coordinates are a measurement of the color distribution created by materials as a function of wavelength (λ) as seen by human brains. As illustrated in Fig. 11(c), the CIE chromaticity coordinates are calculated using the PL information of all nanocomposite components in the chromaticity diagram. Color purity is the degree to which the dominant wavelength seems to predominate in the light. It is computed by comparing the distance between the (x, y) color coordinates and the CIE white illuminants of 1931. The following relationship is used to calculate color purity [32],

$$\text{Color purity} = \frac{\sqrt{(x - x_i)^2 + (y - y_i)^2}}{\sqrt{(x_d - x_i)^2 + (y_d - y_i)^2}} \times 100\% \quad (12)$$

where (x, y) represent the coordinates of the synthesized materials, (x_i, y_i) represent the coordinates of the reference white illumination point, and (x_d, y_d) represent the coordinates of the dominant wavelength. The CIE value and color purity of the synthesized materials are tabulated in the table no. 4. The color purity of the optimized gZ15 composite showed 63.4 %. The nanocomposites color correlated temperature (CCT) values were calculated using McCamy's formula, which is presented below [33, 34],

$$CCT = -437n^3 + 3525n^2 - 6823n + 5520.23 \quad (13)$$

Where, $n = (x - x_e)/(y - y_e)$ is the inverse slope line with (x, y) being the CIE color coordinates and $x_e = 0.3320$, $y_e = 0.1858$ as the epicenter. Color correlated temperature (CCT) is regarded as an important feature that quantifies the appearance/performance of a light source in common parlance. If the CCT value is less than 3200 K, the lights are considered warm, and bulbs with CCT values more than 4000 K are considered cool. Temperatures in the middle of this range are considered neutral in appearance. Using this formula the CCT value of the ZnS was calculated as 4287 K. The CCT value of the composites increases which are more than 10 thousand.

Table 4: CIE, color purity and Duv value of synthesized materials.

Synthesized Material	CIE (x, y)	Purity (%)	Duv
g-C ₃ N ₄ (g)	(0.1702, 0.1806)	69.5	-0.0552
ZnS (Z)	(0.3572, 0.4017)	27.8	0.0188
gZ5	(0.1802, 0.2105)	62.8	-0.0448
gZ10	(0.1822, 0.2251)	60.5	-0.0448
gZ15	(0.1786, 0.2100)	63.4	-0.0460
gZ20	(0.1996, 0.2398)	53.3	-0.0344

All of the findings from the optical study indicated that the composites were suitable materials for the active or emissive layer in optoelectronic devices.

4 Conclusion

The thermal condensation method was used to synthesize g-C₃N₄-ZnS composites, whereas the solvothermal approach was used to synthesize ZnS. The formation of the pure host, filler, and their composites was confirmed by XRD and FTIR analyses. The optimized sample gZ15 has a crystallite size of 4.2 nm and a micro stain of 35.42×10^{-3} . ZnS was displayed as a nanosheets, with the composites evenly distributed over the surface of the sheet. The presence and purity of the components were verified by EDX analysis and the proportion of elements included in the composites. In the preceding discussion section, HR-TEM images of the pure and optimized samples were shown, confirming the composites' development. XPS analysis was used to calculate the oxidation and binding energy of the elements contained in the composite. Due to the presence of ZnS in the composites, which revealed an endothermic reaction, the gZ15 had a higher thermal stability than the host. The optimized material's binding energy was 2.98 eV, with an Urbach energy of 333.3 meV. The refractive index of the materials was computed, and the value for the gZ15 was 2.044. With a purity of 63.4, the photoluminescence displayed a nice intense peak in the visible blue area. The cct value indicated cold light with a high recombination rate. All of the material's characteristics indicated that it is an excellent choice for the active layer (emissive layer) of an optoelectronic device.

Notes

The authors disclose that they have no competing financial interests.

Acknowledgment

The authors would like to express their appreciation to the Indian Institute of Technology (Indian School of Mines), Dhanbad, India, for providing financial assistance as well as experimental and characterization facilities.

Data availability

Data supporting the findings of this study in this publication are accessible upon reasonable request from the corresponding author.

References

- [1] B. Huang, G. Clark, E. Navarro-Moratalla, D.R. Klein, R. Cheng, K.L. Seyler, D. Zhong, E. Schmidgall, M.A. McGuire, D.H. Cobden, W. Yao, D. Xiao, P. Jarillo-Herrero, and X. Xu. Layer-dependent ferromagnetism in a van der waals crystal down to the monolayer limit. *Nature*, 546(7657):270–273, 2017. doi: 10.1038/nature22391. cited By 1802.
- [2] Ye Zhang, Yiguo Xu, Jia Guo, Xiuwen Zhang, Xinling Liu, Yushuang Fu, Feng Zhang, Chunyang Ma, Zhe Shi, Rui Cao, and Han Zhang. Designing of 0d/2d mixed-dimensional van der waals heterojunction over ultrathin g-c3n4 for high-performance flexible self-powered photodetector. *Chemical Engineering Journal*, 420:129556, 2021. ISSN 1385-8947. doi: <https://doi.org/10.1016/j.cej.2021.129556>.
- [3] H. Yu, Y. Xue, and Y. Li. Graphdiyne and its assembly architectures: Synthesis, functionalization, and applications. *Advanced Materials*, 31(42), 2019. doi: 10.1002/adma.201803101. cited By 92.
- [4] Ruey-Chi Wang, Yun-Chen Lin, Hsiu-Cheng Chen, and Wun-Yun Lin. Energy harvesting from g-c3n4 piezoelectric nanogenerators. *Nano Energy*, 83:105743, 2021. ISSN 2211-2855. doi: <https://doi.org/10.1016/j.nanoen.2021.105743>.
- [5] K. Sarkar and Praveen Kumar. Activated hybrid g-c3n4/porous gan heterojunction for tunable self-powered and broadband photodetection. *Applied Surface Science*, 566:150695, 2021. ISSN 0169-4332. doi: <https://doi.org/10.1016/j.apsusc.2021.150695>.
- [6] Baskaran Palanivel, Chinnadurai Ayappan, Venkatesan Jayaraman, Siva Chidambaram, Rathinam Maheswaran, and Alagiri Mani. Inverse spinel nife2o4 deposited g-c3n4 nanosheet for enhanced visible light photocatalytic activity. *Materials Science in Semiconductor Processing*, 100:87–97, 2019.
- [7] P Velusamy, M Sathiya, Yunpeng Liu, Shanhu Liu, R Ramesh Babu, Mohamed Aly Saad Aly, E Elangovan, Haibo Chang, Liqun Mao, and Ruimin Xing. Investigating the effect of nd3+ dopant and the formation of g-c3n4/bioi heterostructure on the microstructural, optical and photoelectrocatalytic properties of g-c3n4. *Applied Surface Science*, 561:150082, 2021.
- [8] Jun Gao, Yong Zhou, Zhaosheng Li, Shicheng Yan, Nanyan Wang, and Zhigang Zou. High-yield synthesis of millimetre-long, semiconducting carbon nitride nanotubes with intense photoluminescence emission and reproducible photoconductivity. *Nanoscale*, 4(12):3687–3692, 2012.
- [9] J. Ma, C. Wang, and H. He. Enhanced photocatalytic oxidation of no over g-c3n4-tio2 under uv and visible light. *Applied Catalysis B: Environmental*, 184:28–34, 2016. doi: 10.1016/j.apcatb.2015.11.013. cited By 223.
- [10] Sridharan Balu, Yi-Lun Chen, R.-C. Juang, Thomas C.-K. Yang, and Joon Ching Juan. Morphology-controlled synthesis of α -fe2o3 nanocrystals impregnated on g-c3n4-so3h with ultrafast charge separation for photoreduction of cr (vi) under visible light. *Environmental Pollution*, 267:115491, 2020. ISSN 0269-7491. doi: <https://doi.org/10.1016/j.envpol.2020.115491>.

- [11] Gohar Ali, Syed Jazib Abbas Zaidi, Muhammad Abdul Basit, and Tae Joo Park. Synergetic performance of systematically designed g-c3n4/rgo/sno2 nanocomposite for photodegradation of rhodamine-b dye. *Applied Surface Science*, 570:151140, 2021. ISSN 0169-4332. doi: <https://doi.org/10.1016/j.apsusc.2021.151140>.
- [12] Salman Ali, Sumaiya Saleem, Muhammad Salman, and Majid Khan. Synthesis, structural and optical properties of zns-zno nanocomposites. *Materials Chemistry and Physics*, 248:122900, 2020. ISSN 0254-0584. doi: <https://doi.org/10.1016/j.matchemphys.2020.122900>.
- [13] Pule V. Raleaooa, Andreas Roodt, Gugu G. Mhlongo, David E. Motaung, Robin E. Kroon, and Odireleng M. Ntwaeaborwa. Luminescent, magnetic and optical properties of zno-zns nanocomposites. *Physica B: Condensed Matter*, 507:13–20, 2017. ISSN 0921-4526. doi: <https://doi.org/10.1016/j.physb.2016.11.031>.
- [14] K. Vasudevan, M.C. Divyasree, and K. Chandrasekharan. Enhanced nonlinear optical properties of zns nanoparticles in 1d polymer photonic crystal cavity. *Optics & Laser Technology*, 114:35–39, 2019. ISSN 0030-3992. doi: <https://doi.org/10.1016/j.optlastec.2019.01.027>.
- [15] G. Palanisamy, Nora Hamad Al-Shaalan, K. Bhuvaneshwari, G. Bharathi, G. Bharath, T. Pazhanivel, Sathishkumar V E, Madan Kumar Arumugam, S.K. Khadeer Pasha, Mohamed A. Habila, and Adel El-Marghany. An efficient and magnetically recoverable g-c3n4/zns/cofe2o4 nanocomposite for sustainable photodegradation of organic dye under uv-visible light illumination. *Environmental Research*, 201:111429, 2021. ISSN 0013-9351. doi: <https://doi.org/10.1016/j.envres.2021.111429>.
- [16] Kai Dai, Jiali Lv, Jinfeng Zhang, Changhao Liang, and Guangping Zhu. Band structure engineering design of g-c3n4/zns/sns2 ternary heterojunction visible-light photocatalyst with zns as electron transport buffer material. *Journal of Alloys and Compounds*, 778:215–223, 2019. ISSN 0925-8388. doi: <https://doi.org/10.1016/j.jallcom.2018.11.127>.
- [17] Arnab Ghosh, Himanshu Saini, Arijit Sarkar, Puspendu Guha, Aneeya K. Samantara, Ranjit Thapa, Suman Mandal, Ajoy Mandal, J.N. Behera, Samit K. Ray, and Dipak K. Goswami. Nitrogen vacancy and hydrogen substitution mediated tunable optoelectronic properties of g-c3n4 2d layered structures: Applications towards blue led to broad-band photodetection. *Applied Surface Science*, 556:149773, 2021. ISSN 0169-4332. doi: <https://doi.org/10.1016/j.apsusc.2021.149773>.
- [18] Taeyoung Song, Jun Young Cheong, Hyunjin Cho, Il-Doo Kim, and Duk Young Jeon. Mixture of quantum dots and zns nanoparticles as emissive layer for improved quantum dots light emitting diodes. *RSC Adv.*, 9:15177–15183, 2019. doi: [10.1039/C9RA01462D](https://doi.org/10.1039/C9RA01462D).
- [19] Pavan P. Gotipamul, Ganesh Vattikondala, Karthik Dilly Rajan, Shweta Khanna, Maheswaran Rathinam, and Siva Chidambaram. Impact of piezoelectric effect on the heterogeneous visible photocatalysis of g-c3n4/ag/zno tricomponent. *Chemosphere*, 287:132298, 2022. ISSN 0045-6535. doi: <https://doi.org/10.1016/j.chemosphere.2021.132298>.
- [20] A. Jesu Jebathew, M. Karunakaran, Mohd Shkir, H. Algarni, S. AlFaify, Aslam Khan, Najla Alotaibi, and Thamraa Alshahrani. High sensitive samarium-doped zns thin films for photo-detector applications. *Optical Materials*, 122:111649, 2021. ISSN 0925-3467. doi: <https://doi.org/10.1016/j.optmat.2021.111649>.

- [21] Mohtaram Danish and Mohammad Muneer. Excellent visible-light-driven ni-zns/g-c3n4 photocatalyst for enhanced pollutants degradation performance: Insight into the photocatalytic mechanism and adsorption isotherm. *Applied Surface Science*, 563:150262, 2021. ISSN 0169-4332. doi: <https://doi.org/10.1016/j.apsusc.2021.150262>.
- [22] Arun Kumar, Samrat Mukherjee, Sanjay Sahare, and Ravi Kant Choubey. Influence of deposition time on the properties of zns/p-si heterostructures. *Materials Science in Semiconductor Processing*, 122:105471, 2021. ISSN 1369-8001. doi: <https://doi.org/10.1016/j.mssp.2020.105471>.
- [23] Zhongwei Fan, Jingfei Luan, Changqing Zhu, and Fuqiang Liu. Depositing ag₂s quantum dots as electron mediators in sns₂/g-c3n₄ nanosheet composites for constructing z-scheme heterojunction with enhanced photocatalytic performance. *Materials Research Bulletin*, 133:111045, 2021.
- [24] Hossein Fattahimoghaddam, Tahereh Mahvelati-Shamsabadi, and Byeong-Kyu Lee. Efficient photodegradation of rhodamine b and tetracycline over robust and green g-c3n4 nanostructures: supramolecular design. *Journal of Hazardous Materials*, 403:123703, 2021.
- [25] Hilal Medetalibeyoğlu. An investigation on development of a molecular imprinted sensor with graphitic carbon nitride (gc₃n₄) quantum dots for detection of acetaminophen. *Carbon Letters*, pages 1–12, 2021.
- [26] G Palanisamy, Nora Hamad Al-Shaalan, K Bhuvaneshwari, G Bharathi, G Bharath, T Pazhanivel, VE Sathishkumar, Madan Kumar Arumugam, SK Khadeer Pasha, Mohamed A Habila, et al. An efficient and magnetically recoverable g-c3n4/zns/cofe₂o₄ nanocomposite for sustainable photodegradation of organic dye under uv-visible light illumination. *Environmental Research*, page 111429, 2021.
- [27] David Ramírez-Ortega, Ana B. Ramos, Agileo Hernández-Gordillo, Rodolfo Zanella, and Sandra E. Rodil. Enhancing the photocatalytic activity of cd-zns(en)_{0.5} hybrid sheets for the h₂ production. *International Journal of Hydrogen Energy*, 45(55):30496–30510, 2020. ISSN 0360-3199. doi: <https://doi.org/10.1016/j.ijhydene.2020.08.049>.
- [28] Sanjeev Kumar and Ram Bilash Choudhary. Influence of mno₂ nanoparticles on the optical properties of polypyrrole matrix. *Materials Science in Semiconductor Processing*, 139:106322, 2022. ISSN 1369-8001. doi: <https://doi.org/10.1016/j.mssp.2021.106322>.
- [29] Sasank Pattnaik and Vineet Kumar Rai. Insight into the spectroscopic and thermometric properties of titanate phosphors via a novel co-excited laser system. *Materials Science and Engineering: B*, 272:115318, 2021. ISSN 0921-5107. doi: <https://doi.org/10.1016/j.mseb.2021.115318>.
- [30] Imran Aslam, M. Hassan Farooq, Usman Ghani, M. Rizwan, Ghulam Nabi, Waseem Shahzad, and Rajender Boddula. Synthesis of novel g-c3n4 microrods: A metal-free visible-light-driven photocatalyst. *Materials Science for Energy Technologies*, 2(3):401–407, 2019. ISSN 2589-2991. doi: <https://doi.org/10.1016/j.mset.2019.04.008>.

- [31] Valerio Sarritzu, Nicola Sestu, Daniela Marongiu, Xueqing Chang, Sofia Masi, Aurora Rizzo, Silvia Colella, Francesco Quochi, Michele Saba, Andrea Mura, et al. Optical determination of shockley-read-hall and interface recombination currents in hybrid perovskites. *Scientific reports*, 7(1):1–10, 2017.
- [32] Debashish Nayak and Ram Bilash Choudhary. Augmented optical and electrical properties of pmma-zns nanocomposites as emissive layer for oled applications. *Optical Materials*, 91: 470–481, 2019. ISSN 0925-3467. doi: <https://doi.org/10.1016/j.optmat.2019.03.040>.
- [33] Sumara Khursheed, Pankaj Biswas, Vivek K. Singh, Vinay Kumar, H.C. Swart, and Jitendra Sharma. Synthesis and optical studies of kcavo4:sm3+/pmma nanocomposites. *Vacuum*, 159: 414–422, 2019. ISSN 0042-207X. doi: <https://doi.org/10.1016/j.vacuum.2018.10.069>.
- [34] Ram Bilash Choudhary and Debashish Nayak. Tailoring the properties of 2-d rgo-ppy-zns nanocomposite as emissive layer for oleds. *Optik*, 231:166336, 2021. ISSN 0030-4026. doi: <https://doi.org/10.1016/j.ijleo.2021.166336>.